

METIS Sensitivity model

Document no.: E-TRE-MET-503-0062

Issue: 1.0

Date: 13 November 2009

Prepared by: Sarah Kendrew

Approved by:

1	Introduction	5
1.1	Summary and Scope	5
1.2	Applicable and reference documents	5
2	Background and method	6
2.1	Inputs and assumptions	6
2.1.1	Wavelength coverage	6
2.1.2	Thermal background	6
2.1.3	Site	8
2.1.4	S/N reference area	8
2.1.5	Adaptive optics	10
2.1.6	Sources	11
2.1.7	Detectors	13
2.2	Equations and symbols	13
2.2.1	Basic inputs	14
2.2.2	Counts from the astronomical source (n_{obj})	15
2.2.3	Counts from the background (n_{sky})	16
3	METIS observation modes	16
3.1	Imaging	16
3.1.1	Optical design	16
3.1.2	Filters	17
3.1.3	Throughput	17
3.1.4	Integration times	18
3.2	Medium-resolution spectroscopy	18
3.2.1	Optical design	18
3.2.2	S/N reference area	19
3.2.3	Grisms	19
3.2.4	Throughput	20
3.2.5	Integration times	20



3.3	High-resolution spectroscopy	20
3.3.1	Optical design	21
3.3.2	S/N reference area	21
3.3.3	Throughput	22
3.3.4	Integration times	23
4	Sensitivity results	23
4.1	Imaging	23
4.2	Medium-resolution spectroscopy	23
4.3	High-resolution spectroscopy	24
5	Discussion	24
5.1	Integration and exposure times	24
5.1.1	Bright sources	25
5.1.2	Chopping and nodding	25
5.2	E-ELT site	26
5.3	Telescope emissivity	26
5.4	AO mode	28



List of Figures

1	Mid-infrared transmission profiles for low and a high site.	8
2	Sky and telescope background fluxes at high and low sites.	9
3	Diagram illustrating the geometry used to convert the square S/N size to the appropriate LTAO circular radius.	11
4	Ensquared energies for METIS in SCAO mode (solid line), compared with the LTAO values(dashed line), for L, M and N bands. The overplotted vertical dotted lines show λ/D for the central wavelengths of the broad-band imaging filters used in the sensitivity model (see Table 4).	12
5	Simulated image of a disk of exozodiacal dust with an integrated flux of 3 mJy at 11 μ m.	12
6	Detector QE for the two METIS science detectors covering L, M and N band. The dashed line is the N band detector, solid line for LM band. Based on manufacturer data for uncoated detectors.	13
7	Pixel sampling properties for the METIS imager channels.	17
8	Effect of rectangular geometry of the S/N reference area in medium-resolution mode.	19
9	Instrumental throughputs of METIS in medium-resolution spectroscopy mode.	20
10	As-designed resolving power in the high-resolution spectrograph in METIS.	22
11	Throughputs for the high-resolution spectroscopy mode in L, M and N bands.	22
12	Atmospheric radiance in M-band around the 4.7 μ m CO emission band for low and high sites.	27
13	Top panel - METIS high-resolution lines sensitivities across L and M bands, for Paranal (+) and a high & dry (*) site. Bottom panel - ratio low:high, showing clearly how the benefit of a high site is greater near the band edges.	27
14	Imaging sensitivities for METIS for telescope emissivities between 10 and 30 %	29

List of Tables

1	Definition of wavelength bands, as used throughout the sensitivity calculations.	6
2	Site characteristics used in generation of transmission and radiance profiles.	8
3	Detector characteristics (per pixel).	13
4	METIS imager filter definitions for the sensitivity calculations.	18
5	Grisms for the medium-resolution spectroscopy mode for METIS.	20
6	Pixel scales in the high-resolution spectroscopy mode.	21



7	METIS imaging sensitivities for L, M and N bands at low and high sites using SCAO. .	23
8	METIS medium-resolution spectroscopic sensitivities for L, M and N bands at low and high sites. Calculated for an unresolved point and line sources observed for 1 hour to S/N of 10.	24
9	METIS high-resolution spectroscopic line sensitivities for L, M and N bands, at low and high sites and for point and extended sources.	24
10	Typical detector integration times (DITs) per observation mode, band and site.	25
11	Object flux at which the object counts within the central pixel reach 10% of the sky flux, requiring downward adjustment of the DIT to avoid saturation.	25
12	Comparison of ensquared energy values between SCAO and LTAO for the S/N reference areas for each mode and band of observation.	30



Change record

Version	Date	Pages/sections affected	Remarks
0.1	30/09/09	all	created
0.9	27/10/09	sec 2.1	added entrance window background and updated results accordingly
1.0	13/11/09	sec 5.2, 5.3	edited text on site discussion. replaced some figures by more colourful versions.

1 Introduction

This document will show the results from the METIS sensitivity model developed in the course of the Phase A study, and present projected sensitivities for METIS in its various observation modes.

We use the model to study the effect of key parameters on the performance of the instrument:

- E-ELT site characteristics
- Telescope emissivity

As such, this report supports and provides background to the documentation set provided at the Phase A final review.

1.1 Summary and Scope

This document details the method of calculation of the performance of METIS in its various modes of operation. We do not include coronagraphic performance. We discuss the sensitivity of METIS to various environmental parameters, such as the E-ELT site, telescope emissivity and AO mode.

1.2 Applicable and reference documents

Applicable Documents

- AD1. J. C. Gonzalez, E-ELT Interfaces for scientific instruments, E-TRE-ESO-582-0252 v. 2, (12/06/09)
- AD2. R. Siebenmorgen, Call for proposals for a Phase A study for a mid-infrared instrument for the E-ELT: Specifications of the instrument to be studied, E-SPE-ESO-503-0115, v.1 (11/11/09)
- AD3. L. Venema, METIS Opto-mechanical design and analysis, E-TRE-MET-503-0010, v.1.7 (04/11/09)
- AD4. S. Hippler, METIS AO Design and analysis report, E-TRE-MET-503-0014, v.1.5 (02/10/09)

Band	λ_{min} (μm)	λ_{max} (μm)
L	3.0	4.2
M	4.5	5.5
N	7.0	13.8

Table 1: Definition of wavelength bands, as used throughout the sensitivity calculations.

- AD5. E. Pantin, METIS Operational Concepts Definition, E-TRE-MET-503-0017, v. 3.4 (20/10/09)
AD6. B.Brandl, METIS Scientific Analysis Report, E-TRE-MET-503-0004, v. 2.5 (20/10/09)
AD7. E. Pantin, B. Brandl, METIS Detector systems design, E-TRE-MET-503-0012, v. 2.0 (10/11/09)

Reference Documents

- RD1. A. Smette, Private communication (2008)
RD2. J. Liske, E-ELT Imaging ETC: Detailed Description, (www.eso.org)
RD3. J. Liske, E-ELT Spectroscopic ETC: Detailed Description, (www.eso.org)
RD4. B. Swinyard et al., Sensitivity estimates for the mid-infrared instrument (MIRI) on the JWST, Proc. SPIE vol. 5489, pp. 785-793 (2004)

2 Background and method

Background information relevant to the sensitivity of METIS is described here, together with listings of basic assumptions and inputs.

2.1 Inputs and assumptions

2.1.1 Wavelength coverage

METIS will cover the wavelength range from 3.0 to 13.8 μm [AD6], more commonly known as the L, M and N bands. Definition of the bands is shown in Table 1. The baseline design for the high-resolution spectroscopy mode covers just the L and M bands, however as the N band unit is kept as an option, we show here sensitivity results for all three bands in IFU mode. Imaging polarimetry is offered only in N band.

2.1.2 Thermal background

The thermal background is of crucial importance in the performance of infrared instruments, both in space and on the ground. Ground-based instruments are however particularly affected by the high

level of background radiation from the atmosphere and the telescope. Dealing with these contributions appropriately is key to the accurate calculation of METIS' performance; particularly given the stipulation that METIS should operate in a background-limited regime (BLIP) in all bands and observation modes [AD2]. Three factors contribute to the thermal background seen at the METIS detector:

- Atmosphere
- Telescope
- Instrument

For the instrumental background we model only the background radiation from the entrance window. This window will consist of an approximately 1.2 cm plate of ZnSe, whose emissivity rises strongly between 12 and 20 μm . As the window will effectively be at ambient temperature, this can add a non-negligible background component in the N band. Our models show however that the contribution of the entrance window is small, thanks to transmission properties of the dichroics, which filter out most radiation longward of 20 μm .

The atmosphere acts as a strong radiator at IR wavelengths; the emissivity profile depends on the vertical profiles of temperature, pressure and molecular abundances (e.g. H_2O , CO , CH_4), and the telescope's altitude above sea level. In these calculations we reference two different scenarios for the E-ELT site, (i) a Paranal-like "low", and (ii) a 5000-m "high and dry" site. Characteristics of these sites are shown in section 2.1.3. Atmospheric emissivity profiles were provided to the community by ESO, these were calculated by A. Smette (ESO) using the Reference Forward Model with the HITRAN 2004 molecular database, assuming a model tropical atmosphere and including the most common atmospheric molecules H_2O , CO , CO_2 , CH_4 , O_2 , O_3 and N_2O [RD1]. These profiles were produced with $R \sim 100000$, and they were subsequently convolved to lower resolutions of 100, 3000 and 50000 for use in the imager, medium-resolution spectroscopy and N-band IFU spectroscopy calculations, respectively.

The atmosphere also affects the sensitivity calculations in that its molecular constituents (and aerosols) absorb IR radiation from astronomical sources. Transmission profiles were generated by ESO using the same tools for the emissivity profiles and provided to the community through the Design Reference Mission initiative. The transmission profiles at the two considered sites are shown in Fig. 1.

The telescope itself radiates as a grey body, at a temperature assumed equal to the ambient temperature appropriate to the site (see Table 2. The telescope emissivity was specified by ESO to be $\leq 10\%$ [AD1], however, this value is assumed to be a lower limit given (i) the segmented design of the primary mirror and contribution of the inter-segment gaps; (ii) the presence of dust; (iii) reflectivity variations between segments; and (iv) the effect of any missing segments. The effect on the sensitivity of an increased telescope emissivity was studied using the sensitivity model, and the results are discussed in section 5.3.

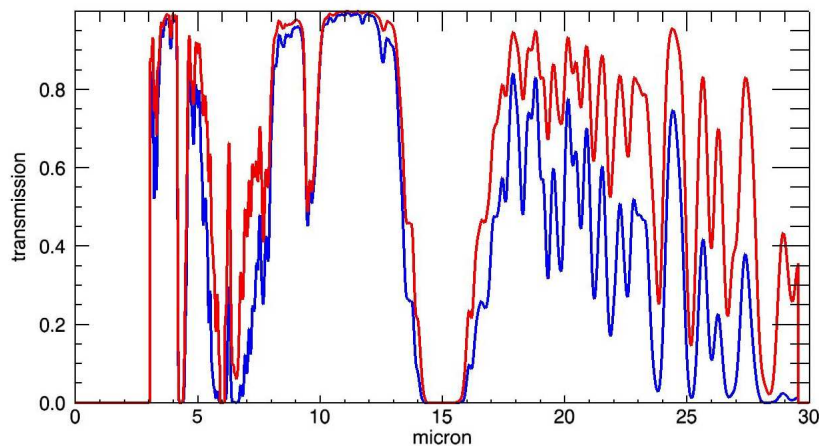


Figure 1: Mid-infrared transmission profiles for low and a high site.

Site	Altitude (m)	Temperature (K)	pwv (mm)
Paranal	2600	286.	2.3
High & dry	5000	270.	0.5

Table 2: Site characteristics used in generation of transmission and radiance profiles.

2.1.3 Site

Throughout these calculations, we reference two different sites, representing possible choices of site for the E-ELT. Characteristics of these sites are shown in Table 2. A discussion of the difference in performance of METIS to be expected at the different sites was an important goal of this activity, and conclusions from the sensitivity results at the two sites are discussed in section 5.2. To give an idea of the difference in external background flux at the two sites, Fig. 2 shows the background flux at (but outside) the instrument from both the telescope and sky, for both sites considered.

2.1.4 S/N reference area

The sensitivity values shown in this document are calculated over a S/N reference area, which essentially represents the area over which the photons from an unresolved point source are spread on the detector. The size of this region is relevant in determining the detector noise contribution to the total noise, on the one hand, and the determination of ensquared or encircled energy fraction in the target signal, on the other. In general we have employed a square geometry for the S/N area and similarly reference the ensquared, rather than encircled, energy from the PSF. As a rule of thumb the S/N area is taken to be the size of the diffraction limited core at the central wavelength of observation.

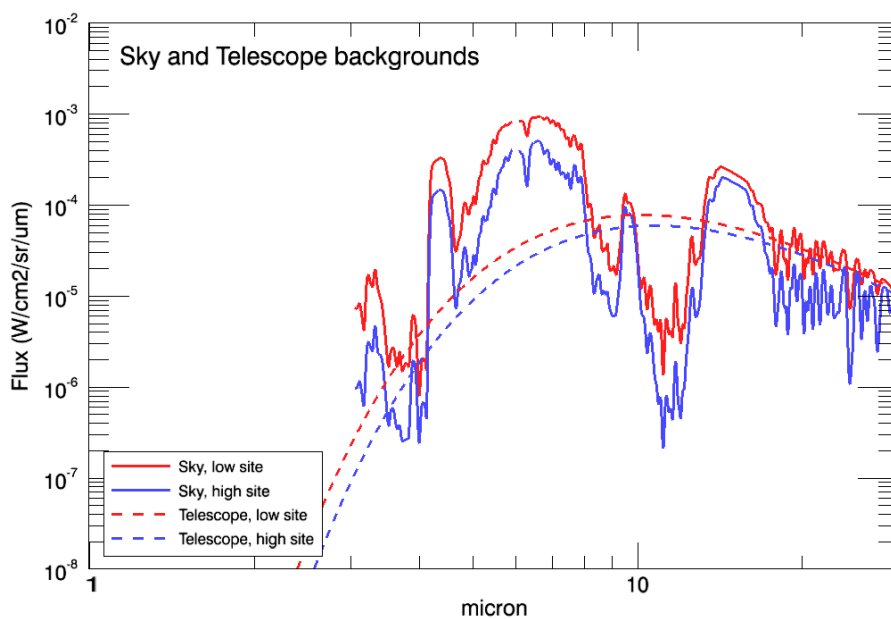


Figure 2: Sky and telescope background fluxes at high and low sites.

The exact definition of the S/N reference area, however, varies between the different modes of observation of METIS, and the calculation method is described for each mode in section 3.

2.1.5 Adaptive optics

METIS will use adaptive optics (AO) to achieve diffraction-limited performance. The baseline mode of operation uses single-conjugate adaptive optics (SCAO), with a single natural guide star as reference source. Two laser tomography AO (LTAO) units are also under study for the E-ELT and this mode could also be of use to METIS if and when they become available. Using data provided by the LTAO study teams we compare the performance of METIS in SCAO and LTAO modes in section 5.4.

The key parameter in the sensitivity calculations defining the quality of the AO correction is the ensquared energy parameter ee . This defines the amount of energy that is contained within the S/N reference area (roughly corresponding to the size of the diffraction limited PSF); the higher the ee percentage, the more photons are concentrated in the central region of the PSF and the better the instrument's ability to detect the source.

For SCAO the ensquared energies were calculated by L. Jolissaint using modelling code PAOLA. The simulations assumed seeing of 0.65'' at a zenith angle of 30° (giving a line-of-sight seeing of 0.71''), an outer scale of 25 m (ref doc - AO inputs) and a guide star V-band magnitude of ≤ 10 . We assume the same AO performance at the low and high sites.

For comparison, we also calculated sensitivities for the LTAO case using performance calculations carried out by the ATLAS consortium, and provided to the METIS team for reference. These numbers however give the encircled, rather than ensquared, energies for given radii from the centre of the PSF. We therefore have to convert these numbers to the appropriate square size for a comparison with the SCAO performance of METIS.

The geometry for this is shown in Fig. 3: for a given square width R_{sq} of the S/N reference area, we can use either the encircled energy within an inner (radius R'_c) or an outer circle (radius R_c). The diagram shows that the percentage energy contained in the inner circle is lower than the ensquared energy for R_{sq} , and that in the outer circle is higher. We therefore use both conversion and take the average of these values as representative LTAO performance for METIS. Using the symbols shown in the figure:

$$\begin{aligned} R_c &= R_{sq}/\sqrt{2} \\ R'_c &= R_{sq}/2 \end{aligned}$$

Fig. 4 shows the SCAO ensquared energy from the PAOLA simulation compared with the equivalent LTAO number, calculated as explained above. The reference wavelengths for the calculations were 3.7 μm , 4.85 μm and 10.45 μm for SCAO, and 3.45 μm , 4.7 μm and 10.0 μm for LTAO. For the best comparison these should ideally be matched, however, the uncertainties incurred by these small discrepancies are assumed to be negligible. Note that the number of available data points was limited

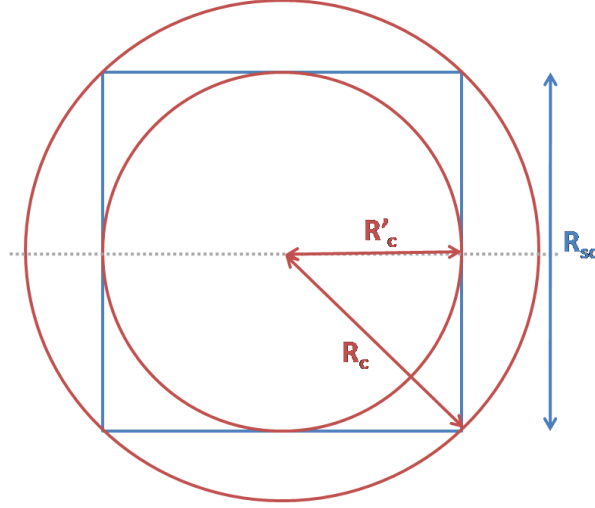


Figure 3: Diagram illustrating the geometry used to convert the square S/N size to the appropriate LTAO circular radius.

from the LTAO simulations, particularly in the region beyond 50 mas, which is relevant for the N-band. This can introduce significant uncertainty in the sensitivity calculation for METIS in LTAO mode.

2.1.6 Sources

To calculate sensitivities some general assumptions on the input source are needed. Broadly speaking a source can be either resolved or unresolved. The majority of sensitivity values presented in this document assume the source is unresolved, i.e. is a point source.

Given the high angular resolution of the E-ELT, however, many of METIS' science targets are likely to be resolved by the instrument. We therefore also examine the extended source sensitivity for a few representative cases for the imager and IFU modes.

Imager For the imager we take a concrete example from the science case [AD6], an exozodiacal dust disk (see Fig. 5), as prototype extended source for METIS. We ignore the presence of the central hole and define a half-light radius R_h for the disk of $0.1''$. We then calculate the imaging sensitivity within the circular area defined by R_h , i.e. $sn\ size = \pi R_h^2$. Given the definition of R_h , the encircled energy in this case is 0.5.

IFU For the IFU with its smaller field of view we assume a constant surface brightness target that covers the entire field (i.e. size of target \gg field of view). In this case the encircled energy becomes a redundant parameter, and both the sky background (n_{sky}) and object flux (n_{obj}) are computed within the same S/N reference area.

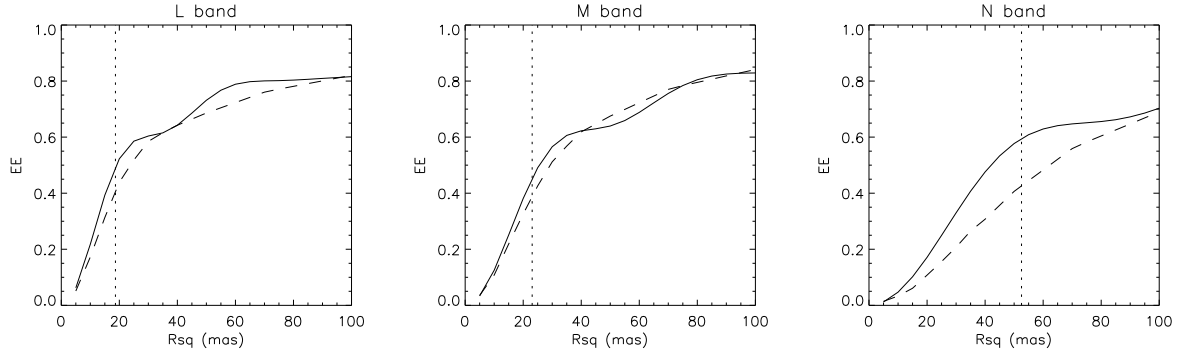


Figure 4: Ensquared energies for METIS in SCAO mode (solid line), compared with the LTAO values (dashed line), for L, M and N bands. The overplotted vertical dotted lines show λ/D for the central wavelengths of the broad-band imaging filters used in the sensitivity model (see Table 4).

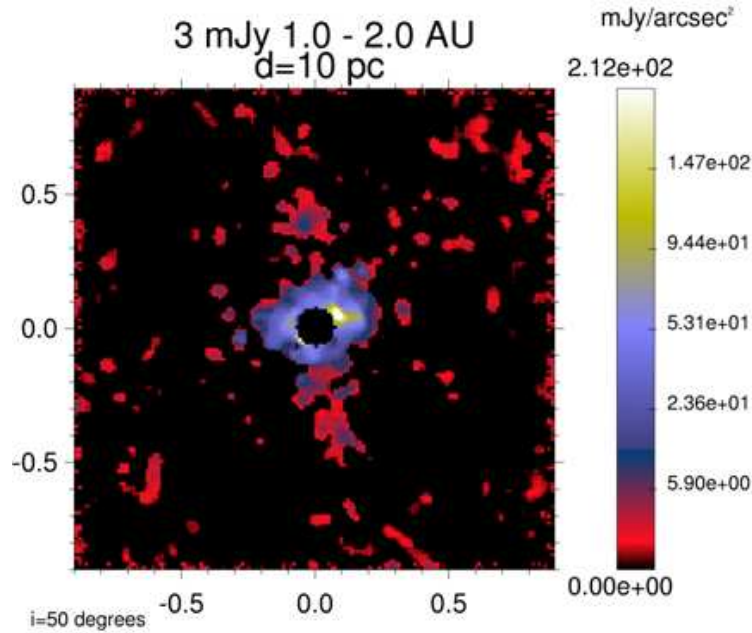


Figure 5: Simulated image of a disk of exozodiacal dust with an integrated flux of 3 mJy at 11 μm located in an annulus between 1 and 2 AU from a solar type star located at 10 pc from the sun, as seen by ELT-METIS at 11 m in the phase mask coronagraph mode. This simulated source was used as a template for extended source sensitivity calculations for the METIS imager.

	LM band	N band
no. pixels	2k x 2k	1k x 1k
pixel size (μm)	18	30
dark current (e-/s)	0.5	2000
read noise (e-/frame)	20	1000
well depth	120,000	1.4e+7

Table 3: Detector characteristics (per pixel).

2.1.7 Detectors

Three different detectors will be used in METIS. The (optical) CCD in the internal wavefront sensor unit is not of relevance here and will not be discussed. For L and M band observations the proposed detector is a 2k x 2k Teledyne (HgCdTe) Hawaii-II detector, for N band a 1k x 1k Raytheon Aquarius (Si:As) detector is foreseen. The specifications as relevant to the sensitivity calculations are listed in Table 3. Detector quantum efficiencies were modelled using manufacturer data, see Fig. 6 [AD7].

The data presented in the plot are representative of uncoated detectors. To simulate the presence of an anti-reflection coating, we apply an improvement factor of 1.2 to the DQE. Photo-conductive gain (*pcg*), the multiplicative factor between photons and electrons, is assumed to be 1.0.

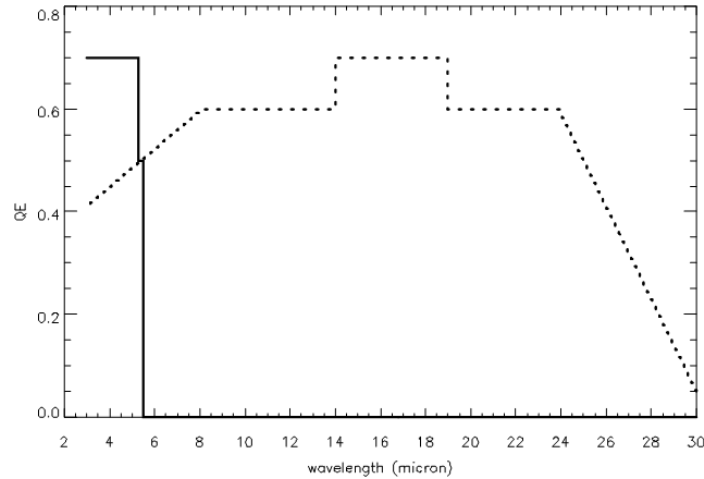


Figure 6: Detector QE for the two METIS science detectors covering L, M and N band. The dashed line is the N band detector, solid line for LM band. Based on manufacturer data for uncoated detectors.

2.2 Equations and symbols

In this section we describe the equations used to calculate the sensitivity of METIS. These follow the procedures described in RD2, RD3 and RD4.

The S/N relation underlying the calculation is:

$$S/N = \frac{\sqrt{frames} \times n_{obj}}{\sqrt{n_{obj} + n_{sky} + n_{pix} \times (rd)^2 + n_{pix} \times (dark) \times (DIT)}} \quad (1)$$

where:

frames = number of frames per exposure

DIT = detector integration time per frame [s]

n_{obj} = detector counts from the object in the S/N reference area [e-/s]

n_{sky} = detector counts from the sky background in the S/N reference area [e-/s]

n_{pix} = number of pixels in the S/N reference area, determined by sampling properties of the observing mode

rd = detector read noise per pixel [e-/frame]

dark = detector dark current per pixel [e-/s]

Ignoring the noise contribution of the source ($\sqrt{n_{obj}}$), the sensitivity can be calculated as the minimum detectable signal at a S/N of 10 in a 1 hour exposure:

$$minsig = \frac{S/N \times \sqrt{n_{sky} + n_{pix} \times (rd)^2 + n_{pix} \times (dark) \times (DIT)}}{\sqrt{frames}} \quad [e-] \quad (2)$$

which can be converted back into flux units. We can now expand, first on some basic inputs related to the telescope and detectors, then on the calculation of key parameters in eqns 1 and 2.

The sensitivity model is set up such that both the S/N for a given source and the sensitivity at S/N can be produced as output. The source flux F_{obj} must be specified in milli-Jansky (mJy) and is assumed to be constant with wavelength within the wavelength region of the observation (i.e. within the filter bandwidth).

2.2.1 Basic inputs

Photon energy at wavelength λ (E_γ) = $1.985 \times 10^{-19} / \lambda$ [J/ γ]

primary mirror area = $\pi \times (21)^2 = 1385.4 \text{ m}^2$

central obscuration = 9.2% of primary area = $0.092 \times 1385.4 = 127.5 \text{ m}^2$

total effective collecting area (A) = $1385.4 - 127.5 = 12.6 \times 10^2 \text{ m}^2 = 12.6 \times 10^6 \text{ cm}^2$

telescope mirror reflectivity = 98%

telescope transmission (τ_{tel}) = $0.98^5 = 0.903$

A factor that enters both the calculation of source and background signals is $conv$, defined as the conversion factor between incident photon flux at the telescope to detected photo-electrons. This factor is calculated as follows:

$$conv = \frac{\tau_{tel} \times \tau_{ins} \times (dqe) \times (pcg) \times \Delta\lambda}{E_\gamma} \quad [e-/s \text{ per } W/cm^2/\mu m] \quad (3)$$

where

τ_{ins} = instrument throughput (see section 3 for discussion of throughputs in the different instrument configurations)

τ_{tel} = telescope transmission, as above

dqe = detector quantum efficiency (see section 2.1.7)

pcg = photo-conductive gain = 1

$\Delta\lambda$ = filter width or width of resolution element, see section 3.

The product of telescope transmission, instrument throughput, detector quantum efficiency and photo-conductive gain can be seen as the overall "efficiency" of the instrument.

2.2.2 Counts from the astronomical source (n_{obj})

For an unresolved point source, the number of electron counts at the detector from the astronomical source, within the defined S/N reference area, is given by:

$$n_{obj} = F'_{obj} \times (ee) \times (conv) \times (DIT) \quad [e-/DIT] \quad (4)$$

where ee and $conv$ are as defined above, and:

F'_{obj} = the flux from the source arriving *at the telescope*, given by $\tau_{atm} \times F_{obj}$, where τ_{atm} is the atmospheric transmission and F_{obj} the source flux at the top of the atmosphere [$W/cm^2/\mu m$]

ee = the encircled energy, i.e. the fraction of energy from the source radiation within the S/N reference area. This quantity is obtained from lookup tables from AO simulations.

2.2.3 Counts from the background (n_{sky})

The detector counts from the thermal background within the S/N reference area per exposure can be calculated from:

$$n_{sky} = F_{sky} \times \Omega \times (conv) \times (DIT) \quad [e-/DIT] \quad (5)$$

where:

F_{sky} = the flux from the thermal background [$W/m^2/\mu m/arcsec^2$], defined as sky emissivity $\times \tau_{tel}$ + telescope background + entrance window background. The sky, telescope and window emissivity models are described in section 2.1.2.

Ω = size of the S/N reference area [$arcsec^2$]. The S/N reference area is taken to be square in geometry, with $\sqrt{\Omega}$ given by the optical design of the given instrument mode (see section 2.1.4).

3 METIS observation modes

In this section we will discuss each observation mode of METIS individually and describe the mode-specific inputs used in the sensitivity calculation.

3.1 Imaging

The METIS imager consists of two separate channels, one for LM band and one for N band, separated by a dichroic. A slit and grism can be inserted into the optical path to achieve low- to medium-resolution spectroscopy (see section 3.2).

3.1.1 Optical design

The field of view and sampling properties from the optical design of the imager determine the pixel field of view on sky, i.e. how much thermal background is seen by each pixel. In addition, the sampling determines over how many pixels the light from the source PSF is spread, and thus the number of pixels in the S/N reference area.

The imager provides a square field of view of 17.6" squared, with sampling optimised (Nyquist sampled) at 3.5 μm for LM band and 7 μm for N band. The resulting pixel scales are:

- LM band: pix scale = 8.6 mas/pix
- N band: pix scale = 17.2 mas/pix

From these values the size of the S/N reference area and the number of pixels it contains (n_{pix}) can be calculated (see Fig. 7). From the pixel sampling values we calculate the number of pixels over which λ_c/D , where λ_c is the central wavelength of the chosen filter, is spread. The area occupied by these pixels form the square S/N reference area.

$$\begin{aligned} npix &= (\text{ceil}(\lambda_c/D/\text{pix scale}))^2 \\ sn\ size &= npix \times (\text{pix scale})^2 \end{aligned}$$

where $\text{ceil}(x)$ means we round the quotient upwards, i.e. the number of pixels covered will always be the square of a whole number such as 3×3 , 4×4 etc.

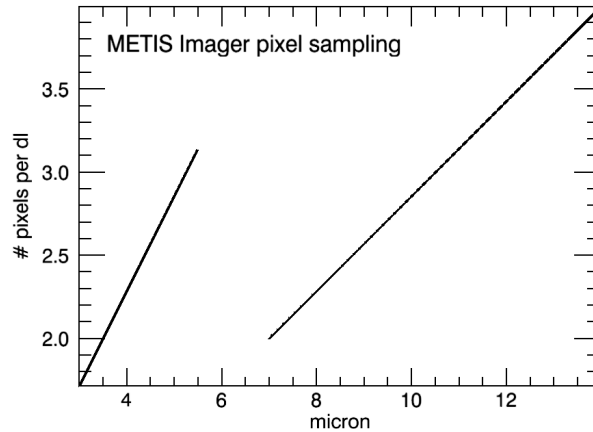


Figure 7: Pixel sampling properties for the METIS imager channels.

3.1.2 Filters

The METIS imager will have a range of broad- and narrow-band filters available to the observer. For the sensitivity calculations we use one representative broad-band filters per band. These are shown in Table 4. A full listing of filters is given in [AD3].

3.1.3 Throughput

The total throughput of the imager was computed in a separate routine using reflectivity of 99% for “regular” reflective optics, and wavelength-dependent transmission profiles for the entrance window

Band	λ_c (μm)	$\Delta\lambda$ (μm)
L	3.78	0.58
M	4.66	0.10
N	10.7	1.40

Table 4: METIS imager filter definitions for the sensitivity calculations.

and dichroics. These profiles are described in more detail in [REF - thermal analysis doc]. The throughputs in the three filters were calculated to be:

- throughput (L) = 0.61
- throughput (M) = 0.58
- throughput (N) = 0.60

i.e. all around 60%.

3.1.4 Integration times

In imaging mode with relatively broad filter bandwidths the background radiation is high and detector pixels quickly saturate. Assume that detector linearity breaks down at approximately half-well, the integration times were calculated to be the time taken for the background electron counts per pixel to reach half the well depth, i.e. from eq 5 and the detector well depths shown in Table 3:

$$DIT = \frac{n_{sky}/n_{pix}}{well/2} \quad [s] \quad (6)$$

Finally, we also apply a 20% overhead factor to the total on-source integration time, such that $frames = 0.8 \times total\ integration\ time / DIT$. We do not take into account any extra duty cycle related to the chopping and nodding; essentially we assume that both the chop and nod mechanisms will keep the source in the field. This is not likely to be the case and the duty cycle could be substantially lower in practice.

3.2 Medium-resolution spectroscopy

The low- to medium-resolution spectroscopy mode in METIS is achieved by inserting a slit and grism into the optical path of the imager. Its optical design parameters are therefore very similar to the imager mode described above.

3.2.1 Optical design

Spatial sampling properties for the medium-resolution spectroscopy mode are the same as for the imager. The slit width is set to $2\lambda_{slit}/D$ at the shortest wavelengths in the band, i.e. $\lambda_{slit} = 3\ \mu m$ and $7\ \mu m$ for LM and N bands, respectively. We assume that a resolution element is sampled by 2 pixels.

3.2.2 S/N reference area

The size of the resolution element was taken to be the rectangular area given by slit width \times the FWHM of the PSF at the central wavelength of observation (λ/D). The deviation from square geometry has no effect on the calculation of sky background counts n_{sky} but will overestimate the ensquared energy. This is illustrated in Fig. 8: the solid line shows λ vs. λ/D for both bands, which would be the assumed length of a side in a square S/N reference area, as in the imager; the dashed line shows λ vs. the square root of the rectangular area assumed for the medium-resolution mode.

This will give an increase in ee of around 5-10% around the band centres and subsequently a similar increase in n_{obj} (see Table 12).

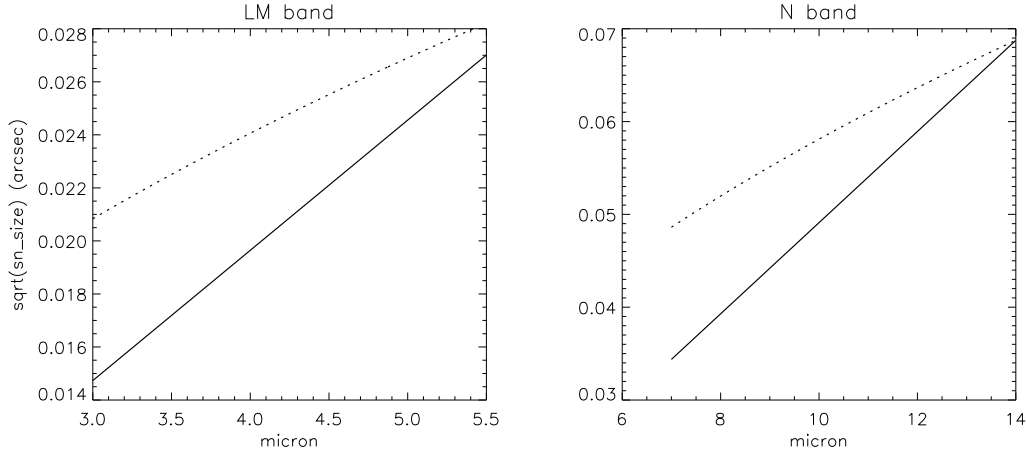


Figure 8: Illustration of effect of rectangular geometry of the S/N reference area in medium-resolution mode. Solid line is λ/D , dashed line is $\sqrt{2 \times \lambda/D \times \lambda/D}$.

The number of pixels in the S/N reference area is calculated using:

$$n_{pix} = \frac{(1.22\lambda/D [mas]) \times (2\lambda/D [mas])}{(pix\ scale [mas/px])^2}$$

3.2.3 Grisms

A number of grisms are proposed for the low- and medium-resolution spectroscopy mode in METIS (for a full listing see [AD3]). For the sensitivity calculation we reference the two lowest-resolution grisms per band, each of which give one-shot full-band coverage for LM and N bands, respectively. The grism details are listed in Table 5.

Band	λ_{min} (μm)	λ_{max} (μm)	2 px resolving power
LM	2.8	5.2	1700
N	8.0	14.0	940

Table 5: Grisms for the medium-resolution spectroscopy mode for METIS.

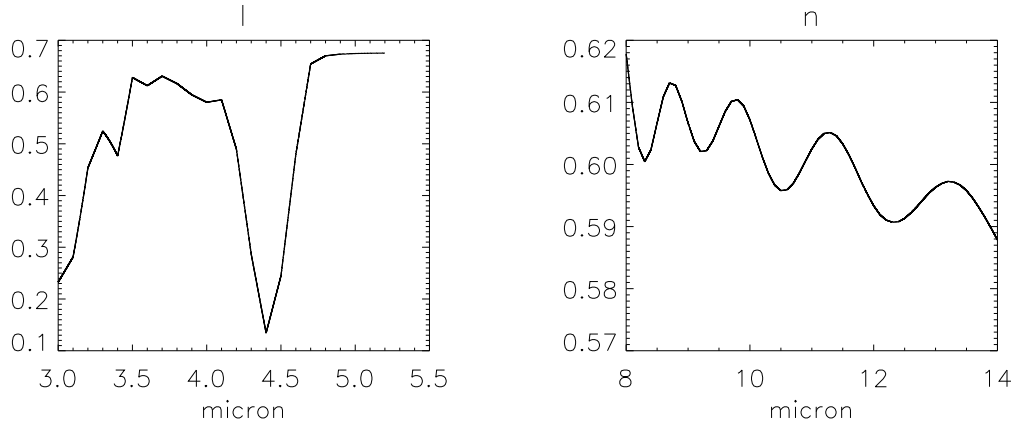


Figure 9: Instrumental throughputs of METIS in medium-resolution spectroscopy mode, for LM band (L) and N band (R), given the grism specifications given in Table 5.

3.2.4 Throughput

The calculation method for the throughput of the medium-resolution spectrograph mode in METIS is essentially the same as that for the imager, with the addition of a grism (ZnSe). Resulting throughput curves are shown in Fig. 9. Also, given the broad band coverage of the grisms, the throughput is also affected by artefacts in the transmission profile of the band-splitting dichroic around 4-4.5 μm . This dichroic transmission profile is based on data from MIRI dichroics via the University of Reading, where these dichroics were procured. This is an active area of research and the transmission is therefore not necessarily representative of the dichroics in METIS.

3.2.5 Integration times

Integration times were calculated in the same way as for the imager mode - see section 3.1.4, with the usual 20 % overhead factor.

3.3 High-resolution spectroscopy

The high-resolution spectrograph in METIS in its baseline design consists of a single channel, separate from the imager and medium-resolution spectrograph optics, covering the L and M bands. An additional channel for the N band is a design option, and we include the details for this optional module

Pixel scale	LM band (mas/px)	N band (mas/px)
spatial	9.0	22.0
spectral	7.2	17.6

Table 6: Pixel scales in the high-resolution spectroscopy mode.

in our sensitivity calculations for reference. The input parameters relevant this mode are discussed below.

3.3.1 Optical design

The spectrograph shares the pre-optics module with the rest of the instrument for image derotation; beyond this the light is split off to a dedicated spectroscopy channel. The spectrograph is an integral field design using an image slicer to divide the field spatially.

In the spatial direction, the slice width is optimised to give critical (Nyquist) sampling at $\lambda_{spat} = 3.7 \mu m$ and $9.0 \mu m$ for LM and N bands respectively, i.e. the number of spatial pixels in the S/N reference area pix_{spat} is given by $2 \times (\lambda / \lambda_{spat})$.

Spectrally the resolving power is designed to be 100,000 for LM band and 50,000 for the N band module. These resolving powers are optimised at the locations of key spectral markers in the relevant wavelength ranges, CO at $4.7 \mu m$ for LM band, and [NeII] at $12.8 \mu m$ for N band. At these locations an unresolved line will be sampled by 2.5 pixels (an anamorphism factor of 1.25 is introduced by the gratings). As the variation of spectral sampling is affected both by the changing resolution element and the wavelength dependence of the dispersion function, we assume 2.5 pixel spectral sampling over the whole band, i.e. $pix_{spec} = 2.5$. This will however not be the case in practice.

The anamorphism essentially gives each pixel a rectangular, rather than square, field of view. Pixel scale in spatial and spectral directions are shown in Table 6.

Wavelength coverage in a single exposure is ~ 60 nm at LM band and ~ 120 nm in N band.

The resolving power is variable with wavelength, which leads to a similar variation in $\Delta\lambda$ (as $\Delta\lambda = R/\lambda$). We use the resolving power obtained from the optical design, see Fig. 10, to take this variation into account.

3.3.2 S/N reference area

From the above discussion we assume that there are n_{pix} in the S/N reference area, where:

$$n_{pix} = pix_{spec} \times pix_{spat} = 2.5 \times 2 \times (\lambda / \lambda_{spat}) \quad (7)$$

The size of the S/N reference area is then calculated from eq. 7 and the pixel scales shown in Table 6.

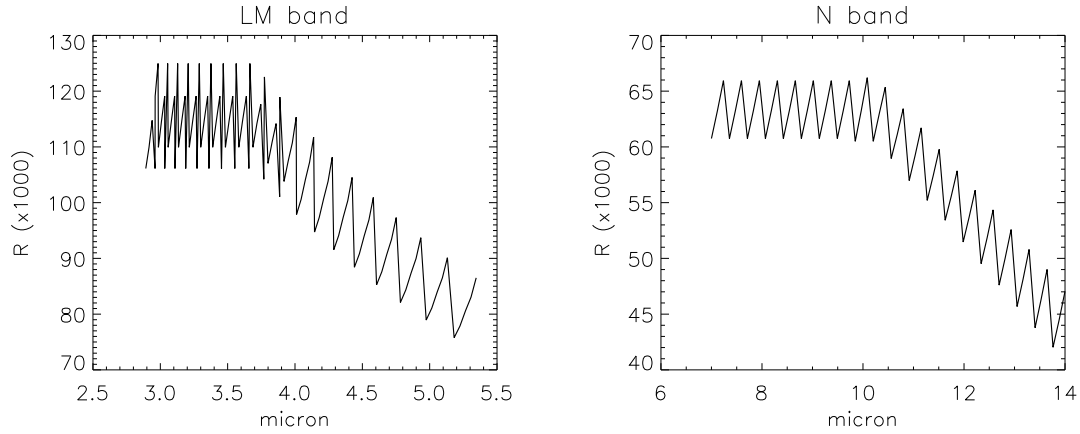


Figure 10: As-designed resolving power in the high-resolution spectrograph in METIS.

3.3.3 Throughput

The high-resolution spectrograph module contains significantly more optical elements than the imager and therefore has a reduced throughput. This calculation is described in detail in REF - thermal analysis doc, and includes contributions from the reflective optics (including the image slicer and those in the pre-optics), dichroics, entrance window, gratings, pre-dispersion prism (ZnSe), and wavelength-dependent slicing loss. For grating efficiency we assume a constant value of 0.85, however, this number is likely to be variable with wavelength in practice and could lead to loss of performance at the band edges. The results of throughput calculations for all three bands is shown in Fig. 11.

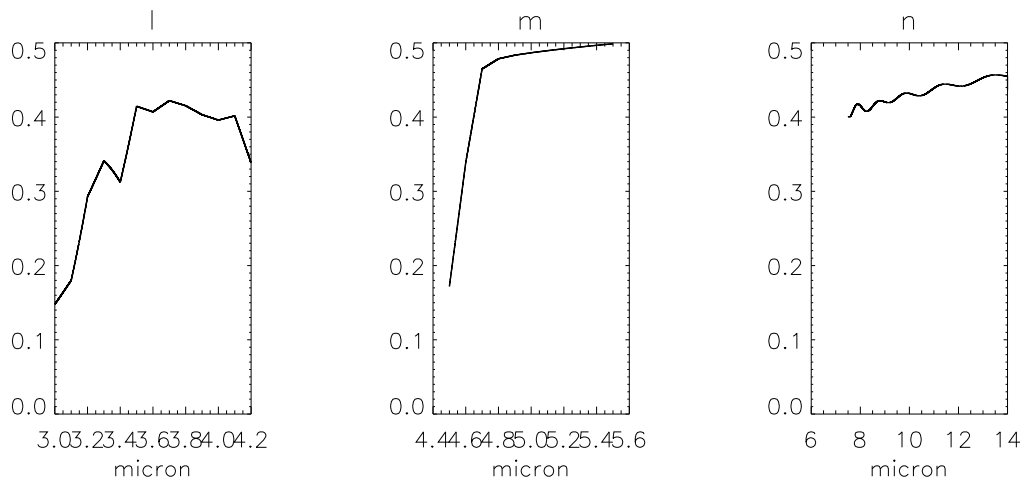


Figure 11: Throughputs for the high-resolution spectroscopy mode in L, M and N bands.

Band	$\lambda_c(\mu m)$	Sensitivity, point (μJy)		Sensitivity, extended (μJy)	
		Low site	High & dry site	Low site	High & dry site
L	3.78	0.6	0.4	5.0	3.0
M	4.66	7.0	4.2	47.0	28.0
N	10.7	27.5	23.0	91.0	76.0

Table 7: METIS imaging sensitivities for L, M and N bands at low and high sites using SCAO. The point sensitivities were calculated for an unresolved point source observed for 1 hour to S/N of 10. Extended source sensitivities give the integrated flux observable within a half-light radius of $0.1''$.

3.3.4 Integration times

Because of the strong dilution of the source and background signals the read noise contribution to the total noise becomes significant. METIS should operate in BLIP mode, i.e. with background noise dominant over detector noise. We therefore calculate the integration time such that the background noise is *twice* the detector read noise.

As in the other modes, we apply an overhead of 20%, i.e. total on-source integration time = $0.8 \times (frames) \times (DIT)$.

4 Sensitivity results

We present here the overview of results from the calculations described above for each of the METIS modes.

*All sensitivities presented here are for a 1-hour exposure (**total** exposure time = $frames \times DIT$) on an unresolved point/line source, as appropriate, to a S/N of 10. They do not take into account any chop/nod duty cycle.*

4.1 Imaging

Imaging sensitivities in representative broad-band filters per band are shown in Table 7 for a low and a high and dry site. Sensitivity to an extended source, using inputs described in section 2.1.6 and calculated at the same reference wavelengths per band as the point source sensitivity, is shown in the same table. Table

4.2 Medium-resolution spectroscopy

Medium-resolution spectroscopic sensitivities are listed in Table 8.

Band	$\lambda_c(\mu m)$	Low site		High site	
		Cont (μJy)	Line ($\times 10^{-19} W/m^2$)	Cont (μJy)	Line ($\times 10^{-19} W/m^2$)
L	4.05	15	0.06	10	0.04
M	4.7	46	0.17	29	0.11
N	12.8	507	1.26	429	1.1

Table 8: METIS medium-resolution spectroscopic sensitivities for L, M and N bands at low and high sites. Calculated for an unresolved point and line sources observed for 1 hour to S/N of 10.

Band	$\lambda_c(\mu m)$	Sensitivity, point ($\times 10^{-19} W/m^2$)		Sensitivity, extended ($\times 10^{-19} W/m^2$)	
		Low site	High & dry site	Low site	High & dry site
L	4.05	0.009	0.006	12.2	8.4
M	4.7	0.026	0.017	21.4	14.5
N	12.8	0.133	0.116	25.6	22.2

Table 9: METIS high-resolution spectroscopic line sensitivities for L, M and N bands, at low and high sites and for point and extended sources. Calculated for an unresolved line observed for 1 hour to S/N of 10.

4.3 High-resolution spectroscopy

High-resolution spectroscopic line sensitivities are shown in Table 9 for unresolved lines detected at S/N of 10 in 1 hour. The table shows results for both point and extended sources. For the extended source we assume the source \gg the field of view.

5 Discussion

5.1 Integration and exposure times

The integration times (DITs) required for METIS to operate in BLIP mode are calculated in the sensitivity computation, and their values give an important insight into METIS' operating conditions.

In summary, for the imager and the medium-resolution spectrometer, where the DIT is determined by the saturation limit of the detector pixels, DIT is calculated to keep the background counts below 50% of the well depth. For the high-resolution mode, the background signal is highly diluted and saturation is no longer a danger, and the biggest noise contributor is the detector read noise. We therefore calculate the DIT to give background counts equalling double the read noise contribution.

The results of these calculations per mode, band and site are listed in Table 10. These values are dependent on chosen filters in case of the imager, and on the central reference wavelength for spectroscopy, and should only be seen as "typical" values.

Band	Site	Imager DIT (s)	Med-res DIT (s)	IFU DIT (s)
L	low	0.2	0.5	38
	high & dry	0.4	1.1	84
M	low	0.2	0.4	8
	high & dry	0.4	1.0	18
N	low	0.03	0.3	48
	high & dry	0.04	0.4	64

Table 10: Typical detector integration times (DITs) per observation mode, band and site.

Band	Low site	High site
	F_{max} (mJy)	F_{max} (mJy)
L	0.1	0.05
M	2.2	0.9
N	230	163

Table 11: Object flux at which the object counts within the central pixel reach 10% of the sky flux, requiring downward adjustment of the DIT to avoid saturation.

5.1.1 Bright sources

In the calculation of imager DITs we assume that the contribution from the science target is negligible compared to the sky background flux. As the brightness of a science target increases, these DITs may need to be reduced to avoid saturation yet; particularly given the high Strehl ratios METIS is expected to reach. We calculate the flux at which the object counts in the brightest pixel reach 10% of the sky background counts, which would necessitate a 10% reduction in DIT, by rearranging equations `refeq:nobj` and 5 and adjusting to account for the single brightest pixel:

$$F_{max} = \frac{0.1 \times F_{sky} \times sn\ size}{n_{pix} \times \tau_{atm} \times ee_c} \quad W/cm^2/\mu m \quad (8)$$

where ee_c is the ensquared energy within the central pixel, whose linear size on sky is defined by the pixel scale. The resulting values for F_{max} can then be converted to Jy units for the central filter wavelength, as listed in Table 4.

The results, listed in Table 11, show that even relatively faint sources ($\sim 100\mu Jy$) will contribute at a 10%-level to the detector counts, particularly at the shortest wavelengths and at a high & dry site.

5.1.2 Chopping and nodding

METIS will employ various background subtraction strategies to remove the thermal background from the frames, using an internal chopper mirror for quasi-traditional chopping. The telescope will be used to nod for removing the changing telescope thermal footprint in the field. The chopping and nodding schemes have not been taken into account in any of these performance calculations.

5.2 E-ELT site

The comparative background plot in Figure 1 indicates qualitatively how the choice of E-ELT site may affect the performance of METIS. The atmospheric background dominates particularly the short edge of the L-band, the M-band and the long-wavelength edge of the N-band. Lower molecular abundances will improve the transparency of the window and lower the atmospheric radiance (e.g. in the CO-bands around $4.7\ \mu\text{m}$, see fig. 12). In other regions, such as the short-wavelength part of the N-band, the telescope background dominates over the atmospheric radiance, and the benefit of a high site derives mainly from the lower ambient temperature.

For spectroscopy, a clear advantage is that even the strongest atmospheric absorption features are no longer saturated at very low humidity (typically above 5000m), allowing the observed spectra to be calibrated for telluric absorption. During periods of very low atmospheric water vapour, the usually opaque $5\text{--}8\ \mu\text{m}$ range can become accessible to ground-based astronomy.

In general, the sensitivity values in Tables 7, 8 and 9 indicate an improvement in L and M band of the order of 30%, and around 15% in N band. These values however generally cover band centres, where the atmospheric windows are at their most transparent. To investigate how the performance differs in the band edges, where atmospheric absorption is stronger, we calculate the high-resolution spectroscopic line sensitivities across the L and M bands for the Paranal and high & dry site cases (see fig. 13).

On inspection of the ratio between the sensitivities at the two sites (bottom panel), we clearly see how the gain at the band edges is indeed higher - up to almost an order of magnitude in the range $3.2\text{--}3.4\ \mu\text{m}$ (L band). Beyond $5\ \mu\text{m}$ in M band the gain at the high site also rises above the band average.

In summary, METIS will be able to meet all its key science goals at a Paranal-like site compared with a high and dry location. Even at a low site, the calculated sensitivities fall well within what is required by the science case. The improved sensitivity at a high site and better transparency at the band edges, however, will increase the sample size available to observing programs, improve the observing efficiency (through shorter integration times), and allow for a more accurate telluric line calibration in spectroscopy.

5.3 Telescope emissivity

It is clear from the discussion so far that the background from sky and telescope are an important, if not the most important, factor on the performance of any mid-IR ground-based instrument. The emissivity of the telescope is of particular concern, as its effect is twofold:

- higher emissivity increases the thermal background seen by the detector; and
- higher emissivity implies a lower reflectivity, which leads to reduced throughput of the system.

This two-part effect of the telescope emissivity means the relationship between telescope emissivity and instrumental performance is not straightforward, depending on the telescope site (i.e. telescope

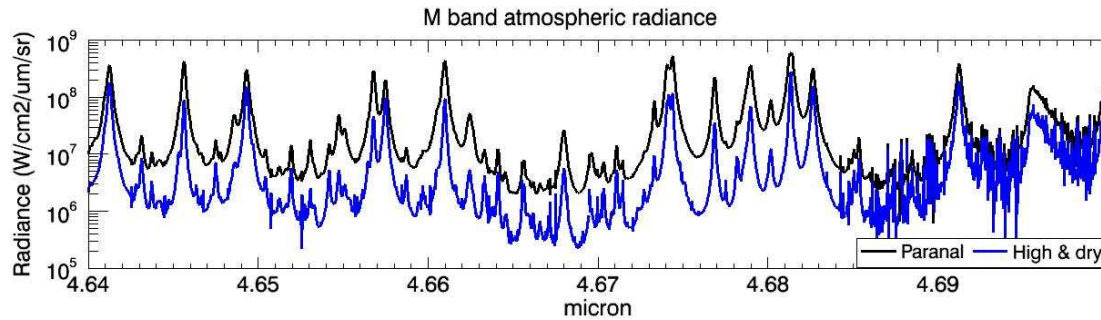


Figure 12: Atmospheric radiance in M-band around the $4.7 \mu\text{m}$ CO emission band for low and high sites.

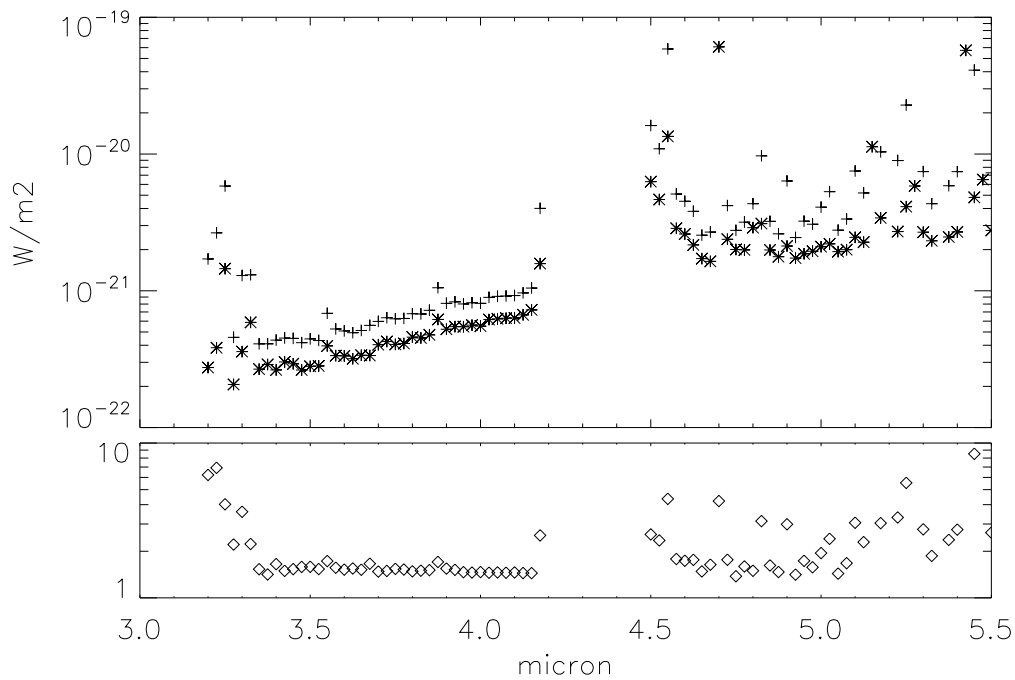


Figure 13: Top panel - METIS high-resolution lines sensitivities across L and M bands, for Paranal (+) and a high & dry (*) site. Bottom panel - ratio low:high, showing clearly how the benefit of a high site is greater near the band edges.

temperature), the wavelength of observations and the filter bandwidth. In terms of the formalism shown in section 2.1.4, the emissivity will reduce the telescope transmission (τ_{tel}) and increase telescope background contribution to n_{sky} .

The emissivity of the telescope is dominated by the emissivity of its largest optical surface, the primary mirror. The value of this parameter will be determined by the reflectivity of the mirror coatings, which may vary substantially between the segments; gaps in between the segments, which will act as strong (near-blackbody) infrared radiators; the presence of dust; and roll-off at the segment edges from the polishing process, which will cause extra light scattering and could potentially reflect warm sources near the telescope into the beam. In our calculations we assume the telescope radiates as a grey body at the ambient temperature of the site, i.e. irrespective of these properties, the telescope's background flux is lower at a high & dry site. The telescope emissivity as specified by ESO [AD1] is $\leq 10\%$.

To test the dependence on telescope emissivity of METIS' sensitivity, we recalculated the sensitivity for telescope emissivity values from 10 to 30 % in imaging mode. The results, shown in Fig. 14, show the following:

- The deterioration of imaging sensitivity is quite dramatic, up to a factor 2 in L and N bands and a factor of 1.6 in M band. The precise value of the loss in sensitivity depends on band, filter and telescope site, however, a high telescope emissivity of 30% will result in a loss of sensitivity of at least 50 and up to 100% at both a high and a low site.
- On comparison with the top level requirements on the imaging sensitivity from the science case (see section 1.2.4 of ADxx), we can stipulate that METIS will only meet (all) these requirements if the telescope emissivity remains $\leq 20\%$ at a low site, and $\leq 25\%$ at a high site. This is driven by the N band, where the infrared thermal background of both atmosphere and telescope is stronger than in L and M bands for a given temperature.

5.4 AO mode

We used performance calculations of the proposed LTAO system for the E-ELT to estimate METIS' sensitivity using LTAO. While SCAO is the baseline AO mode for METIS, LTAO could be used on faint targets that are not bright enough to act as reference sources themselves. Over the small field of view of METIS, SCAO is expected to deliver better performance.

Assuming the source photon noise is negligible $sensitivity \propto 1/ee$. We can use this relation together with the LTAO encircled energy tables to examine the change in performance for METIS using the different AO modes. Table 12 shows a comparison of ensquared energy values for the three modes of METIS, using as reference the S/N reference area size as described in the above sections, together with the ratio between the values, which indicates the effect on the sensitivity.

From the numbers presented, we can conclude that the sensitivity of METIS with LTAO will worsen by 15-20% in L and M band. The deterioration in N band appears higher, particularly in the spectroscopy modes, where the ensquared energies imply an LTAO sensitivity up to 40% worse than with SCAO.

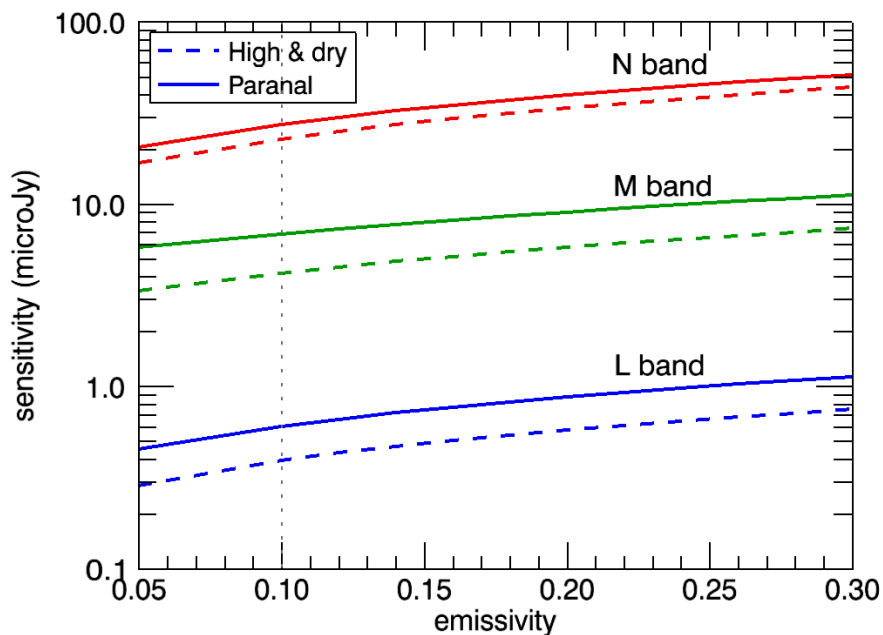


Figure 14: Imaging sensitivities for METIS for telescope emissivities between 5 and 30 %, for L band, M band and N band. The Y-axis shows the absolute sensitivity value.

However, given the low number of data points in the LTAO ee numbers provided at larger distances from the PSF centre, these ees may well be underestimated.

In addition to giving a reduced in ensquared energy, the LTAO mode is also likely to be a less efficient mode of observation, i.e. with larger overheads, to the simpler SCAO configuration.



	Band	ee (SCAO)	ee (LTAO)	ee (SCAO)/ ee (LTAO)
Imager	L	0.586	0.518	1.13
	M	0.491	0.426	1.15
	N	0.647	0.559	1.15
Med-res spec	L	0.586	0.518	1.13
	M	0.491	0.426	1.15
	N	0.641	0.521	1.23
High-res spec	L	0.523	0.44	1.19
	M	0.381	0.326	1.17
	N	0.609	0.445	1.40

Table 12: Comparison of ensquared energy values between SCAO and LTAO for the S/N reference areas for each mode and band of observation.